Quenching a Weyl-Kondo semimetal by magnetic field

Sami Dzsaber[1], Diego A. Zocco[1], Alix McCollam[2], Franziska Weickert[3], Ross McDonald[3], Mathieu Taupin[1], Xinlin Yan[1], Andrey Prokofiev[1], Lucas M. K. Tang[2], Bryan Vlaar[2], Laurel Stritzinger[3], Marcelo Jaime[3], Qimiao Si[4], and Silke Paschen[1,*]

[1]Institute of Solid State Physics, Vienna University of Technology, 1040 Vienna, Austria
[2]High Field Magnet Laboratory (HFML-EMFL), Radboud University, 6525 ED Nijmegen, The Netherlands
[3]Los Alamos National Laboratory, Los Alamos, NM 87545, USA
[4]Department of Physics and Astronomy, Rice Center for Quantum Materials, Rice University, Houston, TX 77005, USA

With the advent of topology in electronic materials the number of predicted quantum phases has literally exploded. Most of them, however, still await firm experimental identification. In strongly correlated electron systems, scanning their low-temperature phase diagrams by varying a nonthermal control parameter has been instrumental in delineating phases defined by a Landau order parameter. Here we show that this approach is versatile also for strongly correlated topological phases. We use Hall effect measurements to probe how the time reversal symmetry invariant Weyl-Kondo semimetal $Ce_3Bi_4Pd_3$ transforms under magnetic-field tuning. We detect an intriguing two-stage transition, which we associate with an annihilation of the Weyl nodes, making the system more insulating, and a consecutive transition to a heavy fermion metal phase. We expect our work to stimulate tuning studies in related systems, thereby advancing the much needed identification of organizing principles for strongly correlated electronic topology.

Significance statement: In condensed matter systems, strong electron correlations not only produce novel phases but also enhance the response to external stimuli. Recently, the quest for topological states driven by correlations has led to the identification of a Weyl-Kondo semimetal in a heavy fermion compound, with remarkable properties. An outstanding question is how this exotic state is stabilized. Paradoxically, this is best studied by suppressing it, which we do here with magnetic fields. We observe an intriguing two-stage transition, with an annihilation of the Weyl nodes that makes the system more insulating and, subsequently, metallic. Our work opens up a new avenue towards understanding the organizing principles for strongly correlated electronic topology and, moreover, points to how strong correlations enable topological functionality.

*Corresponding author. paschen@ifp.tuwien.ac.at

INTRODUCTION

Key to understanding the richness of phenomena displayed by strongly correlated electron systems, ranging from high-temperature superconductivity to colossal magnetoresistance, has been a systematic exploration of their low-temperature phase diagrams [1, 2, 3, 4]. It has lead to the discovery that unconventional, or high-temperature superconductivity is – in many, if not all cases – an emergent phase stabilized by quantum critical fluctuations [5, 6, 7, 8], and that critical electron delocalization transitions [9, 10] may play an important role therein [11, 12]. Such fundamental understanding is indispensable to taylor properties at will, and ultimately exploit them for applications.

A new frontier are materials in which strong electron correlations and topology [13] interplay. Promiment candidates are the pyrochlore iridates [14, 15, 16], Kondo insulators [17] and, most recently, Kondo semimetals [18, 19, 20, 21]. Most studies into these systems have focused on the search for clear signatures of nontrivial electronic topology, which has proven particularly challenging in insulators [22, 23, 24, 25]. For Kondo-driven Weyl semimetals, methods employed to identify Weyl fermions in noninteracting systems, most notably ARPES and the chiral anomaly-induced negative longitudinal magnetoresistance, fail due to the strong bandwidth and quasiparticle velocity renormalisation. As new key characteristics, a giant linear-in-T^3 electronic specific heat [18, 19] and a giant Berry curvature-induced spontaneous Hall effect [21] were demonstrated. These observations set the stage for taking the next step: uncovering the stabilization principles of this exotic phase by inducing transitions to adjacent phases via parameter control.

RESULTS

Here we do so by tuning $Ce_3Bi_4Pd_3$ with magnetic fields. We have performed electrical resistivity, Hall effect, and torque magnetometry measurements in a broad range of temperature and magnetic field. They evidence that, with increasing field, the Weyl nodes annihilate at a first critical field, corresponding to a topological transition into a more insulating state. Then, at a

second critical field, a metallic phase with moderately heavy Fermi liquid behavior forms.

In zero magnetic field, the electrical resistivity of $Ce_3Bi_4Pd_3$ increases weakly with decreasing temperature (Fig. 1A), as observed previously [18]. Note that this behavior cannot be attributed to the presence of an energy gap as a (poor) fit to Arrhenius type behavior yields a gap value that is much lower than the lower cutoff temperature of the fitting range and is thus not meaningful [18]. Instead, the resistivity increase represents semimetallic behavior. The application of magnetic field leads to a gradual suppression of the upturn and, ultimately, to the formation of a metallic state, albeit with higher resistivity than in the nonmagnetic reference compound $La_3Bi_4Pd_3$ (Fig. 1A).

Isothermal measurements of the electrical resistivity (Fig. 1B) and Hall resistivity (Fig. 1C) reveal that this transformation occurs in two stages. The electrical resistivity displays a shoulder at about 9 T and a crossover to almost field-independent behavior at about 14 T, which are both best seen in the lowest-temperature data (Fig. 1B). The Hall resistivity reveals this two-stage transition most clearly. It displays an initial linear increase (see isotherms above 1.9 K; at lower temperatures, a Berry curvature-related contribution is superimposed to it, see Fig. 3A and Fig. S2) up to a maximum, situated near 9 T at the lowest temperature, followed by a steeper negative slope and, at fields above about 14 T, a much weaker field dependence (Fig. 1C). The large (negative) slope at intermediate fields is the signature of an intervening more insulating phase before the system metallizes. We will analyse this behavior quantitatively below, but first present the torque magnetometry results.

At low magnetic fields, essentially no torque signal is detected (Fig. 2A). This is what is expected (see note S1) for a cubic, magnetically isotropic system, with a linear-in-field magnetization. A sizeable torque signal appears only above about 14 T; it corresponds to the onset of nonlinearity in the magnetization (Fig. S1). Similar behavior, albeit with a much larger magnetic field scale, is also seen in the canonical Kondo insulator $Ce_3Bi_4Pt_3$, which we have studied for comparison (Fig. 2B). The onset of sizeable torque produces characteristic signatures in both the first and second derivative of the torque with respect to magnetic field. In the first deriva-

tive, this is a step-like increase which, at the lowest temperatures, reaches half height at 13.5 and 38.9 T for $Ce_3Bi_4Pd_3$ and $Ce_3Bi_4Pt_3$, respectively (Fig. 2C). For $Ce_3Bi_4Pt_3$, this coincides with the Kondo insulator to metal transition evidenced by a jump of the Sommerfeld coefficient between 30 and 40 T [26]. By analogy, we associate the corresponding signature at 13.5 T with the metallization transition in $Ce_3Bi_4Pd_3$, in agreement with the magnetoresistance and Hall resistivity data (Fig. 1B,C). In the second derivative (Fig. 2D), the signature is a maximum, and we use the middle field at half height as characteristic field scale B_τ (Fig. 4A). This analysis shows that the torque signal of $Ce_3Bi_4Pd_3$ only picks up the second transition.

Next, we analyse the Hall resistivity isotherms quantitatively. As established previously [9], when magnetic field drives transitions between ground states with different Fermi volume, the resulting (finite temperature) crossovers manifest as (broadened) kinks in the Hall resistivity $\rho_{xy}(B)$, and (broadened) steps in the differential Hall coefficient $\tilde{R}_{\rm H}(B)$, which is the local slope of $\rho_{xy}(B)$. Such behavior has been observed in a number of heavy fermion metals [9, 27, 28, 29] driven by magnetic field across quantum critical points. The two kinks seen in the $\rho_{xy}(B)$ data of $Ce_3Bi_4Pd_3$ (Fig. 1C) thus evidence two consecutive Fermi volume changing quantum phase transition.

By fitting the data with a phenomenological model [9] (see note S2), in addition to the $\tilde{R}_{\rm H}$ values associated with the different phases, also the crossover fields B^* and their sharpnesses, quantified by the full width at half maximum (FWHM, see note S2), can be extracted. In Fig. 3A,B we show two representative results, at 0.5 and 1.9 K, respectively. Fits of similar quality are obtained at all temperatures up to 10 K (Fig. S2). At higher temperatures, we lose track of the two-stage nature and thus this model does no longer give meaningful results. The temperature-dependent fit parameters are shown in Fig. 3C-F. The two crossover fields B_1^* and B_2^* (Fig. 3B), determined for all available isotherms, are plotted as characteristic temperatures $T_1^*(B)$ and $T_2^*(B)$ in Fig. 3C; in the zero-temperature limit, they extrapolate to $B_{\rm c1}$ and $B_{\rm c2}$, respectively (Fig. 4). Both crossovers sharpen considerably with decreasing temperature (Fig. 3E,F), indicating that the phase diagram of magnetic field-tuned $Ce_3Bi_4Pd_3$ comprises

three phases with distinct Fermi volume: a phase below B_{c1} with a small hole-like Fermi volume, an intermediate-field phase between B_{c1} and B_{c2} with an even smaller electron-like Fermi surface, and a high-field phase beyond B_{c2} with a much larger Fermi volume (Fig. 4B; note that, in the simplest case, the Fermi volume is inversely proportional to $\tilde{R}_{H}$).

None of these three phases appears to be characterized by a Landau order parameter, and thus no finite temperature boundary in the thermodynamic sense can be identified. Instead, we have determined the temperatures up to which characteristics of the different phases are observed (Fig. 4A). For the low-field phase, these are the two key signatures of Weyl-Kondo semimetal behavior evidenced previously, namely the linear-in-T^2 electronic specific heat coefficient C/T [18], observed up to $T_{C/T}$ (Fig. S3), and the Berry curvature-derived Hall resistivity, observed up to T_{H}^{even} in the even-in-field Hall resistivity [21] and up to T_{H}^{odd} in the odd-in-field anomalous Hall effect (Fig. S2 and grey shaded area in Fig.3A).

In the search for a characteristic temperature scale of the metallic high-field phase, we examine the temperature-dependent electrical resistivity of $Ce_3Bi_4Pd_3$. Interestingly, at low temperatures and high fields, $\rho = \rho_0 + AT^2$ behavior is observed (Fig. S4). This form is generally associated with Fermi liquid behavior, where the A coefficient is a measure of the strength of the electronic correlation [30] (only for heavy Fermi liquids is A large enough to be seen against a background from electron-phonon scattering). With decreasing field, A of $Ce_3Bi_4Pd_3$ is at first strongly enhanced, suggesting a divergence near B_{c2} (Fig. 4, right scale). In addition, at 15 T, a non-Fermi liquid linear-in-temperature law holds above 0.8 K (Fig. S5). Such behavior is evidence for a quantum critical point situated at B_{c2}. However, close to this field, a rapid suppression of A is seen and finally a crossover to T^2 behavior with a negative slope (Fig. S4), which we associate with the intermediate insulating phase. Because the drop of the A coefficient is caused by the nearby insulating phase it should not be interpreted in a Fermi liquid picture. Caution is also due when determining the upper boundary of Fermi liquid behavior, T_{FL}, as delineating the Fermi liquid state. In Fig. 4 we therefore report T_{FL} values only in the range of minor influence of the insulating phase. These indicate that the heavy Fermi liquid

phase exists only at fields above B_{c2}.

DISCUSSION

$Ce_3Bi_4Pd_3$ is emerging as a prototype material where strong correlations and electronic topology interplay. Having established the structure of its field-tuned phase diagram allows to address the pertinent questions: What is the nature of the different phases we have delineated and what are the mechanisms stabilizing them? Which design strategies for strongly correlated topological phases can be derived from the new understanding?

The semimetallic phase at low fields has previously been identified, via thermodynamic [18] and transport signatures [21], as a Weyl-Kondo semimetal [19]. The metallic high-field phase shows signatures of a partially field-polarized moderately heavy Fermi liquid. What remains to be clarified is the nature of the intermediate, more insulating phase. The proximity of $Ce_3Bi_4Pd_3$ to a Kondo insulator, realized in $Ce_3Bi_4(Pt_{1-x}Pd_x)_3$ up to at least $x \leq 0.4$ [18], as well as the close similarity of the torque signals of $Ce_3Bi_4Pd_3$ and $Ce_3Bi_4Pt_3$ (Fig. 2C) suggests that this intermediate phase might be a Kondo insulator as well. In fact, magnetic field in Kondo systems is expected to predominantly provide Zeeman coupling, and according to calculations in a magnetic field-tuned Weyl-Kondo semimetal model, a critical field exists where the Weyl nodes annihilate and are thus gapped out [19], thereby giving rise to a topological phase transition [13]. The present study then suggests that the Weyl nodes, which are created in zero field by the inversion symmetry breaking of the noncentrosymmetric crystal structure of $Ce_3Bi_4Pd_3$ and are gapped out at the critical magnetic field B_{c1}, form within the narrow gap of a Kondo insulator. This Kondo insulator then, with further increasing field, collapses to a heavy fermion metal at B_{c2}, just as the Kondo insulator $Ce_3Bi_4Pt_3$ was shown to do at much larger magnetic field [31, 26].

The analysis of the Hall resistivity underpins this interpretation. The charge carrier concentration per Ce, determined at 0.5 K from a simple single-band model, changes from about 0.01 holes in the Weyl-Kondo semimetal, via 0.007 electrons in the more insulating phase, to 0.2 electrons in the heavy fermion metal (Fig. 4B). The application of magnetic field gives rise to

two stages of quantum phase transitions (Fig. 4C). The first transition, that we associate with the annihilation of the Weyl nodes and that hence is topological in nature, leads to a jump in the extrapolated zero-temperature Hall coefficient; this should be further investigated, for instance by thermodynamic probes. The second transition displays signatures of quantum criticality and must thus be nearly continuous. Evidence for quantum criticality at a Kondo insulator to metal transition has previously been seen in pressure-tuned SmB_6 [32, 33]. That similar physics can occur also as function of magnetic field represents and intriguing new subject for future theoretical studies.

Having identified Weyl semimetal behavior in a strongly correlated electron system [18, 21] has allowed us to take advantage of its high tunability to map out its low-temperature phase diagram. We have thus been able to quench a Weyl-Kondo semimetal in two stages of quantum phase transition, annihilating the Weyl nodes in a topological first step that exposes a (Kondo) insulator, and collapsing the (Kondo insulator) gap in a second transition to a (heavy fermion) metal. This sequence is both a confirmation of the Weyl-Kondo semimetal assignment for $Ce_3Bi_4Pd_3$ and a recipe to find other correlation-driven Weyl semimentals in strongly correlated materials and theoretical models in general. Finally, the switching between states distinct in both topological character and carrier density opens new possibilities for applications.

MATERIALS AND METHODS

Synthesis

Single crystals of $Ce_3Bi_4Pd_3$ $Ce_3Bi_4Pt_3$ and of the nonmagnetic reference compound $La_3Bi_4Pd_3$ were grown using a modified Bi flux method, as described in Ref. [18]. The chemical composition and crystal structure of the samples were determined by energy dispersive x-ray spectroscopy and powder x-ray diffraction. Laue diffraction was utilized to determine the crystallographic orientation of selected samples.

High-field experiments

Magnetoresistance, Hall effect, and torque magnetization measurements in DC fields up to 37 T were performed at the HFML-EMFL facility at Nijmegen. Magnetotrasnport data was measured using Stanford Research SR830 lockin amplifiers, with the measured voltage signal pre-amplified 100 times using Princeton Applied Research low-noise transformers. Electrical contacts where made by either spot welding or gluing with silver paint 12 μm diameter gold wires to the samples in a 5-wire configuration.

All displayed Hall resistivity curves were obtained by the standard antisymmetrizing procedure of the resistivity $\rho_{xy}^{\rm meas}$ measured across the Hall contacts, i.e., $\rho_{xy}(B) = [\rho_{xy}^{\rm meas}(+B) - \rho_{xy}^{\rm meas}(-B)]/2$. This cancels out both the spontaneous Hall effect (zero-field signal) and any even-in-field component.

Torque and magnetization measurements in pulsed fields up to 65 T were performed at the NHMFL-LANL facility at Los Alamos. Magnetization data were obtained only for $Ce_3Bi_4Pt_3$, using an extraction magnetometer and the "sample-in/sample-out" technique to separate the sample signal from the background. In this case, the magnetic field was not aligned to any particular crystallographic axis.

In all torque experiments, piezo-cantilevers were used for enhanced sensitivity. Samples were attached to the levers with Dow Corning high vacuum grease. The measured torque signal was obtained after balancing a Wheatstone bridge containing the resistance of the sample's cantilever and a "dummy" (empty lever) resistor. Due to the small samples required for this

technique, the magnetic field was initially not aligned to any particular crystallographic axis. A sample rotator was used to scan the torque signal across different orientations.

In all cases, temperatures down to 0.35 to 0.5 K were obtained using a ^{3}He cryostat.

Low-temperature experiments

Additional magnetoresistance, Hall effect, and specific heat measurements were obtained at TU Vienna using a Quantum Desing Physical Property Measurement System, equipped with ^{3}He options.

Low-temperature electrical resistivity measurements down to 70 mK and in magnetic fields up to 15 T were performed in an Oxford dilution refrigerator.

References

[1] Tokura, Y. & Nagaosa, N. Orbital physics in transition-metal oxides. *Science* **288**, 462 (2000).

[2] v. Löhneysen, H., Rosch, A., Vojta, M. & Wölfle, P. Fermi-liquid instabilities at magnetic quantum critical points. *Rev. Mod. Phys.* **79**, 1015 (2007).

[3] Si, Q. & Steglich, F. Heavy fermions and quantum phase transitions. *Science* **329**, 1161 (2010).

[4] Keimer, B., Kivelson, S. A., Norman, M. R., Uchida, S. & Zaanen, J. From quantum matter to high-temperature superconductivity in copper oxides. *Nature* **518**, 179 (2015).

[5] Mathur, N., Grosche, F., Julian, S., Walker, I., Freye, D., Haselwimmer, R. & Lonzarich, G. Magnetically mediated superconductivity in heavy fermion compounds. *Nature* **394**, 39 (1998).

[6] Scalapino, D. J. A common thread: The pairing interaction for unconventional superconductors. *Rev. Mod. Phys.* **84**, 1383 (2012).

[7] Kuo, H.-H., Chu, J.-H., Palmstrom, J. C., Kivelson, S. A. & Fisher, I. R. Ubiquitous signatures of nematic quantum criticality in optimally doped Fe-based superconductors. *Science* **352**, 958 (2016).

[8] Michon, B., Girod, C., Badoux, S., Kačmarčík, J., Ma, Q., Dragomir, M., Dabkowska, H. A., Gaulin, B. D., Zhou, J.-S., Pyon, S., Takayama, T., Takagi, H., Verret, S., Doiron-Leyraud, N., Marcenat, C., Taillefer, L. & Klein, T. Thermodynamic signatures of quantum criticality in cuprate superconductors. *Nature* **567**, 218 (2019).

[9] Paschen, S., Lühmann, T., Wirth, S., Gegenwart, P., Trovarelli, O., Geibel, C., Steglich, F., Coleman, P. & Si, Q. Hall-effect evolution across a heavy-fermion quantum critical point. *Nature* **432**, 881 (2004).

[10] L. Prochaska, X. Li, D. C. MacFarland, A. M. Andrews, M. Bonta, E. F. Bianco, S. Yazdi, W. Schrenk, H. Detz, A. Limbeck, Q. Si, E. Ringe, G. Strasser, J. Kono, and S. Paschen. Singular charge fluctuations at a magnetic quantum critical point, arXiv:1808.02296.

[11] Badoux, S., Tabis, W., Laliberté, F., Grissonnanche, G., Vignolle, B., Vignolles, D., Béard, J., Bonn, D. A., Hardy, W. N., Liang, R., Doiron-Leyraud, N., Taillefer, L. & Proust, C. Change of carrier density at the pseudogap critical point of a cuprate superconductor. *Nature* **531**, 210 (2016).

[12] Pelc, D., Popčević, P., Požek, M., Greven, M. & Barišić, N. Unusual behavior of cuprates explained by heterogeneous charge localization. *Sci. Adv.* **5**, eaau4538 (2019).

[13] Armitage, N. P., Mele, E. J. & Vishwanath, A. Weyl and Dirac semimetals in three-dimensional solids. *Rev. Mod. Phys.* **90**, 015001 (2018).

[14] Nagaosa, N., Sinova, J., Onoda, S., MacDonald, A. H. & Ong, N. P. Anomalous Hall effect. *Rev. Mod. Phys.* **82**, 1539 (2010).

[15] Wan, X., Turner, A. M., Vishwanath, A. & Savrasov, S. Y. Topological semimetal and Fermi-arc surface states in the electronic structure of pyrochlore iridates. *Phys. Rev. B* **83**, 205101 (2011).

[16] Witczak-Krempa, W. & Kim, Y. B. Topological and magnetic phases of interacting electrons in the pyrochlore iridates. *Phys. Rev. B* **85**, 045124 (2012).

[17] Dzero, M., Sun, K., Galitski, V. & Coleman, P. Topological Kondo insulators. *Phys. Rev. Lett.* **104**, 106408 (2010).

[18] Dzsaber, S., Prochaska, L., Sidorenko, A., Eguchi, G., Svagera, R., Waas, M., Prokofiev, A., Si, Q. & Paschen, S. Kondo insulator to semimetal transformation tuned by spin-orbit coupling. *Phys. Rev. Lett.* **118**, 246601 (2017).

[19] Lai, H.-H., Grefe, S. E., Paschen, S. & Si, Q. Weyl-Kondo semimetal in heavy-fermion systems. *Proc. Natl. Acad. Sci. USA* **115**, 93 (2018).

[20] Guo, C. Y., Wu, F., Wu, Z. Z., Smidman, M., Cao, C., Bostwick, A., Jozwiak, C., Rotenberg, E., Liu, Y., Steglich, F. & Yuan, H. Q. Evidence for Weyl fermions in a canonical heavy-fermion semimetal YbPtBi. *Nat. Commun.* **9**, 4622 (2018).

[21] S. Dzsaber, X. Yan, G. Eguchi, A. Prokofiev, T. Shiroka, P. Blaha, O. Rubel, S. E. Grefe, H.-H. Lai, Q. Si, and S. Paschen. Giant spontaneous Hall effect in a nonmagnetic Weyl-Kondo semimetal; arXiv:1811.02819.

[22] Li, G., Xiang, Z., Yu, F., Asaba, T., Lawson, B., Cai, P., Tinsman, C., Berkley, A., Wolgast, S., Eo, Y. S., Kim, D.-J., Kurdak, C., Allen, J. W., Sun, K., Chen, X. H., Wang, Y. Y., Fisk, Z. & Li, L. Two-dimensional Fermi surfaces in Kondo insulator SmB_6. *Science* **346**, 1208 (2014).

[23] Tan, B. S., Hsu, Y.-T., Zeng, B., Hatnean, M. C., Harrison, N., Zhu, Z., Hartstein, M., Kiourlappou, M., Srivastava, A., Johannes, M. D., Murphy, T. P., Park, J.-H., Balicas, L., Lonzarich, G. G., Balakrishnan, G. & Sebastian, S. E. Unconventional Fermi surface in an insulating state. *Science* **349**, 287–290 (2015).

[24] Xiang, Z., Kasahara, Y., Asaba, T., Lawson, B., Tinsman, C., Chen, L., Sugimoto, K., Kawaguchi, S., Sato, Y., Li, G., Yao, S., Chen, Y. L., Iga, F., Singleton, J., Matsuda, Y. & Li, L. Quantum oscillations of electrical resistivity in an insulator. *Science* **362**, 65–69 (2018).

[25] Liu, E., Sun, Y., Kumar, N., Muechler, L., Sun, A., Jiao, L., Yang, S.-Y., Liu, D., Liang, A., Xu, Q., Kroder, J., Süß, V., Borrmann, H., Shekhar, C., Wang, Z., Xi, C., Wang, W., Schnelle, W., Wirth, S., Chen, Y., Goennenwein, S. T. B. & Felser, C. Giant anomalous Hall effect in a ferromagnetic kagome-lattice semimetal. *Nat. Phys.* **14**, 1125 (2018).

[26] Jaime, M., Movshovich, R., Stewart, G., Beyermann, W., Berisso, M., Hundley, M., Canfield, P. & Sarrao, J. Closing the spin gap in the Kondo insulator $Ce_3Bi_4Pt_3$ at high magnetic fields. *Nature* **405**, 160 (2000).

[27] Friedemann, S., Oeschler, N., Wirth, S., Krellner, C., Geibel, C., Steglich, F., Paschen, S., Kirchner, S. & Si, Q. Fermi-surface collapse and dynamical scaling near a quantum-critical point. *Proc. Natl. Acad. Sci. USA* **107**, 14547 (2010).

[28] Custers, J., Lorenzer, K., Müller, M., Prokofiev, A., Sidorenko, A., Winkler, H., Strydom, A. M., Shimura, Y., Sakakibara, T., Yu, R., Si, Q. & Paschen, S. Destruction of the Kondo effect in the cubic heavy-fermion compound $Ce_3Pd_{20}Si_6$. *Nat. Mater.* **11**, 189 (2012).

[29] Martelli, V., Cai, A., Nica, E. M., Taupin, M., Prokofiev, A., Liu, C.-C., Lai, H.-H., Yu, R., Küchler, R., Strydom, A. M., Geiger, D., Haenel, J., Larrea, J., Si, Q. & Paschen, S. Sequential localization and strange-metal behavior of a complex electron fluid, arXiv:1709.09376.

[30] Kadowaki, K. & Woods, S. B. Universal relationship of the resistivity and specific heat in heavy-fermion compounds. *Solid State Commun.* **58**, 507 (1986).

[31] Boebinger, G. S., Passner, A., Canfield, P. C. & Fisk, Z. Studies of the Kondo insulator $Ce_3Bi_4Pt_3$ in 61 T pulsed magnetic fields. *Physica B* **211**, 227 (1995).

[32] Gabáni, S., Bauer, E., Berger, S., Flachbart, K., Paderno, Y., Paul, C., Pavlík, V. & Shitsevalova, N. Pressure-induced Fermi-liquid behavior in the Kondo insulator SmB_6: Possible transition through a quantum critical point. *Phys. Rev. B* **67**, 172406 (2003).

[33] Zhou, Y., Wu, Q., Rosa, P. F., Yu, R., Guo, J., Yi, W., Zhang, S., Wang, Z., Wang, H., Cai, S., Yang, K., Li, A., Jiang, Z., Zhang, S., Wei, X., Huang, Y., Sun, P., feng Yang, Y., Fisk, Z., Si, Q., Zhao, Z. & Sun, L. Quantum phase transition and destruction of Kondo effect in pressurized SmB_6. *Science Bulletin* **62**, 1439 – 1444 (2017).

Acknowledgements: The authors wish to thank H.-H. Lai and S. Grefe for fruitful discussions. **Funding:** We acknowledge the support of the HFML, member of the European Magnetic Field Laboratory (EMFL). A portion of this work was performed at the National High Magnetic Field Laboratory, which is supported by the National Science Foundation Cooperative Agreement No. DMR-1157490 and DMR-1644779, the State of Florida and the United States Department of Energy. The work in Vienna was supported by the Austrian Science Fund (DK W1243, I2535, I4047, and P29296). The work at Rice was in part supported by the NSF (DMR-1920740) and the Robert A. Welch Foundation (C-1411), the ARO (W911NF-14-1-0525). **Author Contributions:** S.P. designed and guided the research. X.Y. and A.P. synthesized and characterized the material. S.D., D.Z., A.M., F.W., R.M., L.T., B.V., L.S., and M.J. performed the high-field experiments, M.T., S.D. and D.Z. the dilution refrigerator experiments. S.D. analysed the data, with contributions from D.Z., M.T., and S.P. The manuscript was written by S.P., with contributions from S.D. and D.Z. and Q.S. All authors contributed to the discussion. **Competing interests:** The authors declare that they have no competing interests. **Data and materials availability:** All data needed to evaluate the conclusions in the paper are present in the paper and/or the Supplementary Materials. Additional data related to this paper may be requested from the authors.

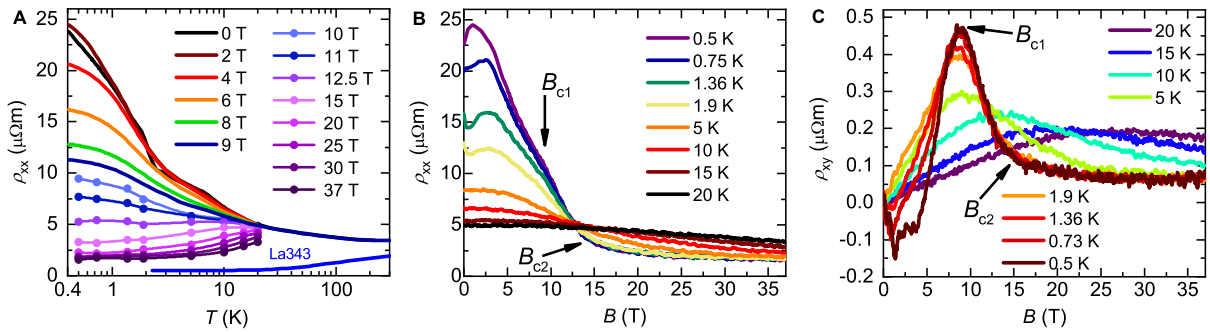

Fig. 1: **High-field magnetotransport of $Ce_3Bi_4Pd_3$.** (**A**) Temperature-dependent electrical resistivity at various fixed magnetic fields. For $B > 9$ T, iso-B cuts (dots) were taken from panel (B). The zero-field resistivity of the nonmagnetic reference compound $La_3Bi_4Pd_3$ is shown for comparison (blue line denoted La343). The low-field data are taken from [21]. (**B**) Magnetoresistance isotherms in fields up to $B = 37$ T, for various temperatures between 0.5 and 20 K. At the lowest temperatures, a shoulder is identified at about 9 T, and a crossover to a very weak field dependence at about 14 T. Arrows indicate the position of the critical fields. (**C**) Hall resistivity isotherms in fields up to $B = 37$ T for the same temperatures. The field dependences, featuring again characteristic signatures at the same two fields, are quantitatively analysed in Fig. 3 and Fig. S2. Arrows indicate the position of the critical fields.

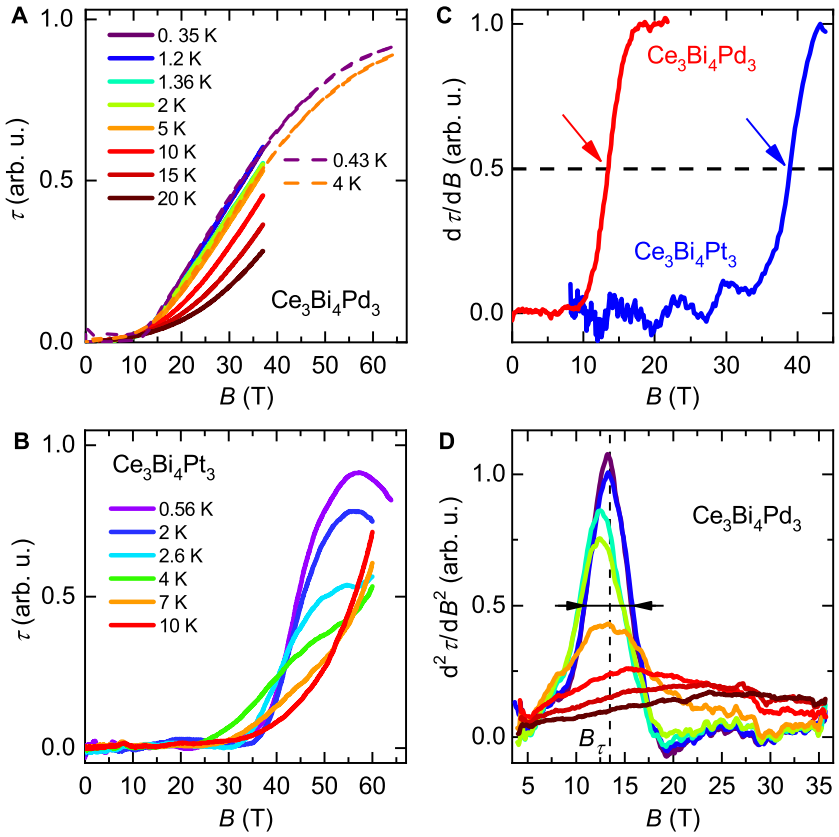

Fig. 2: **High-field torque magnetometry of $Ce_3Bi_4Pd_3$ and $Ce_3Bi_4Pt_3$.** (**A**) Magnetic torque isotherms of $Ce_3Bi_4Pd_3$ at various temperatures as function of applied magnetic field up to 37 T and, for low temperatures, up to 65 T. (**B**) Same as in (A) for the Kondo insulator $Ce_3Bi_4Pt_3$. (**C**) Field derivative of the magnetic torque isotherms of $Ce_3Bi_4Pd_3$ and $Ce_3Bi_4Pt_3$ at the lowest temperatures, revealing similar characteristics, albeit at different fields (the fields where the step-like increases reach half height are indicated by arrows). (**D**) Second field derivative of the torque signal of $Ce_3Bi_4Pd_3$. We define the characteristic field B_τ of the torque signal as the center of the width at half maximum, as indicated by the dashed vertical line and the horizontal arrows for the 0.35 K isotherm.

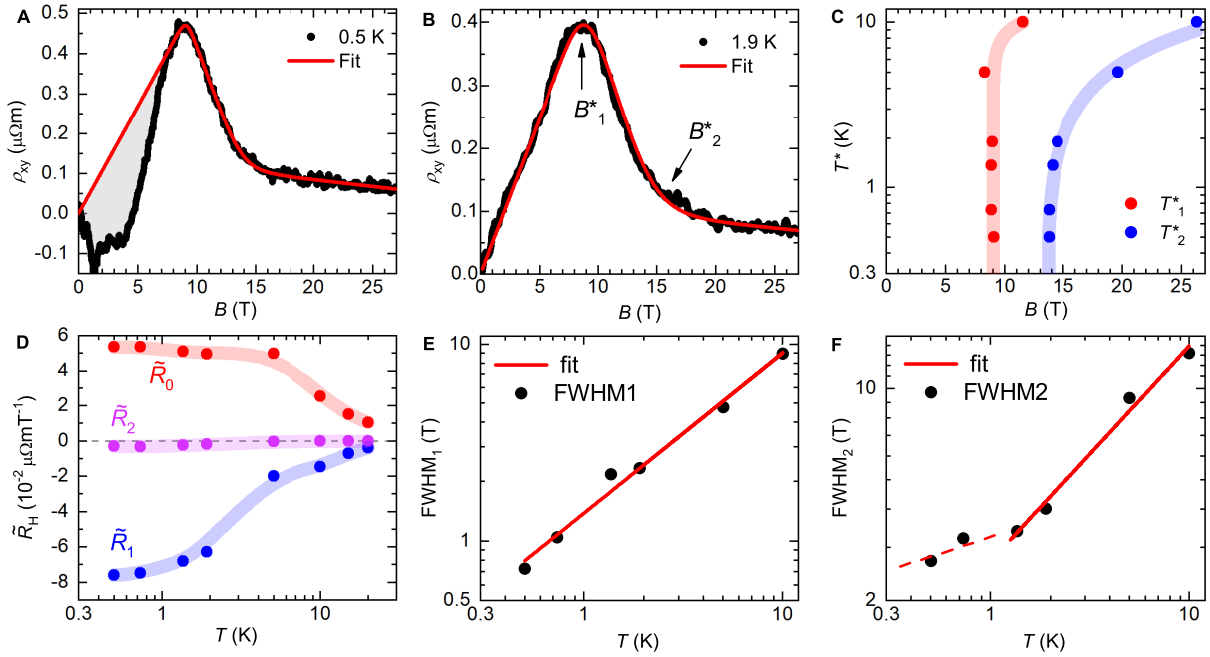

Fig. 3: **Analysis of Hall resistivity isotherms of $Ce_3Bi_4Pd_3$.** (**A**) Hall resistivity vs applied magnetic field at 0.5 K, together with the best fit according to the two-crossovers model (see note S2). The deviation of the data from the initial linear behavior (shaded grey area) is due to the Berry curvature-derived anomalous Hall contribution [21]. (**B**) Same as (A) at 1.9 K. The Berry-curvature derived contribution is essentially absent at this temperature. The two characteristic fields B_1^* and B_2^* mark the positions of the crossovers between the different regimes. (**C**) The crossover fields $B_1^*(T)$ and $B_2^*(T)$ determined from the $\rho_{xy}(B)$ fits are plotted as $T_1^*(B)$ and $T_2^*(B)$, respectively, in a temperature-magnetic field phase diagram. They extrapolate, in the zero-temperature limit, to B_{c1} and B_{c2} (Fig. 4) and separate three regimes of simple (linear-in-B) normal Hall resistivity. (**D**) Differential Hall coefficients $\tilde{R}_0$, $\tilde{R}_1$, and $\tilde{R}_2$ of these three regimes, determined from the $\rho_{xy}(B)$ fits, as function of temperature. The lines are guides to the eyes. (**E**) Width of the first crossover FWHM_1, representing the full width at half maximum of the second derivative of the two-crossovers fit function. The straight line is a pure power law fit, $\mathrm{FWHM}_1 \propto T^p$, with $p = 0.81$. It describes the data down to the lowest temperature, evidencing that the carrier concentration changes abruptly at $T = 0$. (**F**) Same as in (E) for the second crossover. The straight full line is a pure power law fit, $\mathrm{FWHM}_2 \propto T^p$, with $p = 0.71$ to the data above 1 K. At lower temperatures, the rate of decrease is somewhat reduced (red dashed line).

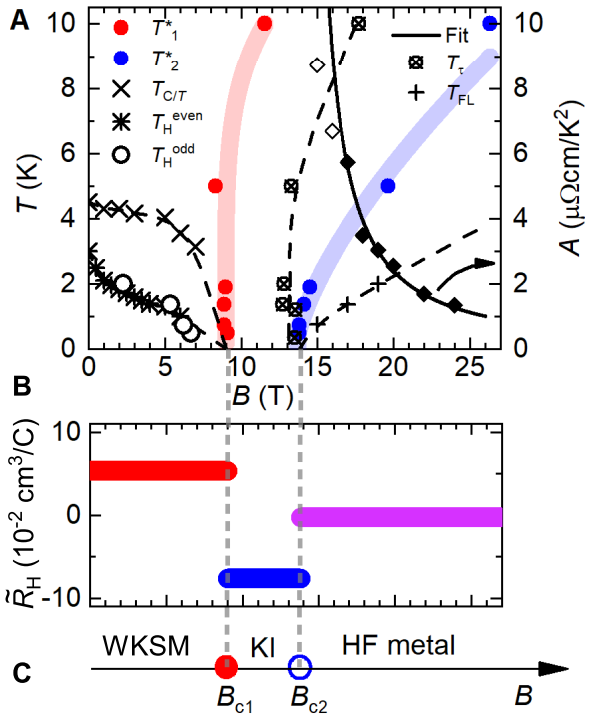

Fig. 4: **Magnetic-field tuned phase diagram of $Ce_3Bi_4Pd_3$.** (**A**) Temperature-magnetic field phase diagram with the crossover temperatures T_1^* and T_2^* from Fig. 3C, the temperature $T_{C/T}$ above which the electronic specific heat coefficient C/T deviates by more than 5% from a low-temperature T^2 law representing the linear Weyl dispersion (Fig. S3), the onset temperature $T_{\rm H}^{\rm even}$ of the Berry curvature-related contribution to the even-in-field Hall resistivity taken from [21], the temperature $T_{\rm H}^{\rm odd}$ below which the Berry curvature-related contribution to the odd-in-field Hall resistivity leads to a deviation of more than 15% from the initial linear-in-B normal Hall resistivity (Fig. S2), the characteristic scale T_τ for the change in character of the torque signal (Fig. 2D), and the temperature $T_{\rm FL}$ above which the data deviate by more that 5% from the Fermi liquid law $\rho = \rho_0 + AT^2$ (all left axis). The A coefficient of this law is plotted on the right axis. Above 16 T, it is well decribed by $A \propto (B - B_{c2})^{-p}$, with $B_{c2} = 13.8$ and $p = 0.985$, suggesting that the effective mass diverges at a quantum critical point situated at B_{c2}. (**B**) Differential Hall coefficient at 0.5 K from Fig. 3D, in the three different regimes. (**C**) Axis across a theoretical zero-temperature phase diagram. The Weyl-Kondo semimetal (WKSM) to Kondo insulator (KI) transition occurs across a quantum phase transition at B_{c1}, the successive insulator to heavy fermion (HF) metal transition occurs across a quantum critical point at B_{c2}.